Applications in Energy and Combustion Science 16 (2023) 100191

Contents lists available at ScienceDirect

Applications in Energy and Combustion Science

journal homepage: www.elsevier.com/locate/jaecs

Large eddy simulation of iron oxide formation in a laboratory spray flame

Fabian Fröde [a,*], Temistocle Grenga [b], Sophie Dupont [c], Reinhold Kneer [c], Ricardo Tischendorf [d], Orlando Massopo [d], Hans-Joachim Schmid [d], Heinz Pitsch [a]

[a] Institute for Combustion Technology, RWTH Aachen University, Templergraben 64, 52056, Aachen, Germany
[b] Faculty of Engineering and Physical Science, University of Southhampton, SO17 1BJ, Southhampton, United Kingdom
[c] Institute of Heat and Mass Transfer, RWTH Aachen University, Augustinerbach 6, 52056, Aachen, Germany
[d] Particle Technology Group, University of Paderborn, Pohlweg 55, 33098, Paderborn, Germany

ARTICLE INFO

Keywords:
Flame spray pyrolysis
Iron oxide formation
Large eddy simulation
Method of moments
SpraySyn

ABSTRACT

Iron oxide nanoparticles are very interesting for many applications in different industrial sectors. A promising process to manufacture these nanoparticles is flame spray pyrolysis (FSP). A lack of understanding of the individual sub-processes in FSP makes it challenging to tailor nanoparticle properties. This work provides insights into the formation of iron oxide nanoparticles in a turbulent spray flame using Large Eddy Simulations (LES), which are based on a comprehensive model, including customized submodels. Highlights are the adaption of a turbulent combustion model and a bivariate hybrid method of moments for modeling nanoparticle dynamics. The work focuses on the SpraySyn burner, which is a standardized laboratory burner and was operated with a precursor-solvent mixture of ethanol and iron(III) nitrate nonahydrate. For studying the relevance of precursor chemistry, LES using an evaporation-limited precursor chemistry model is compared with a model that includes detailed iron chemistry. A further novelty is the inclusion of adsorption in the simulation, which defines a third model for comparison. Sufficient validation is achieved for the undoped LES using experimental data from the literature. A strong impact of the detailed iron chemistry and adsorption is found on the precursor consumption and the aggregate and primary particle formation. Comparing the particle diameters with experimental measurements from the literature and data generated for this work is found unsuitable to asses the precursor chemistry model and revealed an urgent need for future experimental and numerical research. This work serves as a step forward in realizing a reliable model.

1. Introduction

Millions of tons of nanoparticles are produced in flames yearly for many applications in different industrial sectors. While most of these nanoparticles are used in commodity applications serving, for example, as reinforcing agent, pigment, or flowing aid, emerging technologies require more complex and functional nanomaterials. Besides the examples of doped cesium dioxide used in microelectronics and platinum-decorated alumina used in catalysts [1], iron oxide nanoparticles are highly interesting for applications in medical hyperthermia, drug delivery, and protein separation due to their magnetic properties [2–7].

Flame Spray Pyrolysis (FSP) is a promising process to manufacture complex nanoparticles for a wide range of materials, including iron oxide, using low-cost precursors [8,9]. FSP combines the overlapping sub-processes of spray and mixture formation, turbulent combustion, and nanoparticle dynamics. As a result, the overall process is very complex, and a lack of understanding of the individual sub-processes makes it difficult to tailor application-specific nanoparticle properties. In addition to undoubtedly needed experiments, detailed simulations can provide a deep insight into the processes and can be used to enhance designs. Hence, models have been developed to study FSP. Generally, these models can be categorized by the applied turbulence simulation approach, liquid phase modeling, combustion modeling, and nanoparticle dynamics modeling. The following summary focuses on the turbulence simulation approach and nanoparticle dynamics model. The most common approach is the Reynolds-Averaged-Navier–Stokes (RANS) simulation approach. In the RANS works of Gröhn et al. [10], Weise et al. [11], Meierhofer et al. [12], and Torabmostaedi et al. [13,14], the monodisperse model of Kruis et al. [15] was employed. In the model, the entire particle population is replaced by a single particle, and the solution is carried out for the average particle volume and surface area. Consequently, the model belongs to the family of moment-based models. A bivariate (volume and surface area) description of the particle allows for defining aggregate (e.g., aggregate diameter) and

* Corresponding author.
E-mail address: f.froede@itv.rwth-aachen.de (F. Fröde).

https://doi.org/10.1016/j.jaecs.2023.100191
Received 21 April 2023; Received in revised form 2 August 2023; Accepted 9 August 2023
Available online 19 August 2023

primary particle properties (e.g., number of primary particles). The specific surface area of the particles is essential for many applications and strongly depends on the particle morphology. As a result, it is desired to have a model that includes primary particle growth. Even though the monodisperse model features this ability, it is known to underestimate coagulation due to the non-linear coagulation frequency [16,17]. To overcome this, a more advanced closure approach can be used. The Direct Quadrature Method of Moments (DQMOM) [18] was used by Neto et al. [19], and the Hybrid Method of Moments (HMOM) [20] was recently employed by Dasgupta [21] in their RANS simulations.

In contrast to RANS, Large Eddy Simulations (LES) resolve the unsteady large-scale turbulent structures, providing a deeper insight into the process dynamics. The first LES of FSP was performed by Rittler et al. [22], which used a bivariate monodisperse model. Later, Wollny et al. [23] and Sellmann et al. [24] replaced the monodisperse model with a univariate sectional model to study the decoration of alumina with platinum particles and iron oxide formation, respectively. The work of Sellmann et al. is particularly relevant for this work as it focuses on the same burner, operating conditions, and precursor-solvent mixture. Kirchmann et al. [25] performed LES of FSP using a univariate sectional model, which switches from instantaneous coalescence and aggregation using a user-defined diameter. While this includes the distinction between aggregate and primary particle growth, it requires prior knowledge of the primary particle diameter. In addition, surface growth or adsorption is a known growth mechanism, which can be relevant for metal oxides [26]. Nevertheless, none of the models includes adsorption. Hence, this process was not studied in the context of FSP simulation. To summarize, LES of FSP using a bivariate moment-based model with an advanced closure approach including adsorption would provide additional insights into aggregate and primary particle growth.

To unite research activities on FSP, the standardized SpraySyn laboratory burner was established recently [27]. As a standard test case, the production of iron oxide nanoparticles from a precursor-solvent mixture of ethanol, ethylhexanoic acid, and iron(III) nitrate nonahydrate was defined. While ethanol serves as a natural solvent, ethylhexanoic acid was found to improve the precursor-solvent mixture stability [28]. From a modeling perspective, this precursor-solvent mixture poses two substantial challenges. First, to the authors knowledge, there is no validated reaction mechanism for ethylhexanoic acid. Second, it was found that micro-explosions take place with a significant impact on the droplet dynamics [29,30]. As a result, a model for micro-explosions is needed to be able to predict the precursor release correctly. Understanding and modeling micro-explosions is, however, a subject of ongoing research and is not the scope of this work. In addition to the standard precursor-solvent mixture, several studies [24,31,32] used ethanol and iron(III) nitrate nonahydrate as a precursor-solvent mixture for producing iron oxide nanoparticles. While this circumvents the above-mentioned modeling challenges, it was found that undesired large particles are formed via the droplet-to-particle pathway [31]. In the work of Sellmann et al. [24], a relatively low precursor concentration was studied, for which it is likely that the droplet-to-particle route is less relevant. Note that also the physical mechanisms behind the formation of large particles are not fully understood and require further research. As part of that, there is quite poor knowledge about the chemistry inside the droplet, the release of iron species, and the gas phase chemistry. From the experimental works of Stodt et al. [28] and Keller et al. [33], which both focus on liquid phase chemistry, it is known that iron hydroxide forms and precipitates. Reaching equilibrium, however, takes more than 24 h, and for short times after mixing, no precipitating was observed. Hence, it is likely that a mixture of ethanol, water, and dissolved iron(III) nitrate is present. From the experiments of Mu and Perlmutter [34], it is known that iron(III) nitrate starts to decompose at 403.15 K into solid iron oxide. Based on this, Sellmann et al. [24] assumed that iron(III) nitrate decomposes instantaneously, and a mixture of ethanol, water, oxygen, nitrogen dioxide, and iron oxide leaves the droplet. In the gas phase, iron oxide is then consumed and formed again, from which a inception rate is computed.

There is no doubt that further research is required to obtain a fundamental understanding of all the chemical processes taking place. To potentially guide future research, this work aims to study the relevance of precursor chemistry in the particle formation process. For this, a bivariate moment-based LES model is formulated first, which is able to study aggregate and primary particle growth. The model combines customized state-of-the-art sub-models, where the adaption of a turbulent combustion model and the bivariate hybrid method of moments for modeling nanoparticle dynamics are highlighted. The model is then used to compare an evaporation-limited precursor chemistry model with a model that includes detailed iron chemistry. The effect of adsorption is additionally studied using a third model that adds adsorption to the detailed iron chemistry model.

The paper is structured as follows. In Section 2, the experimental configuration and data will be explained. The model is formulated in detail in Section 3, which is followed by a description of the numerical framework and simulation setup in Section 4. In Section 5, the results are presented and discussed. The paper finishes with conclusions in Section 6.

Table 1
Nominal inner (D_in) and outer (D_out) diameter of each stream of the SpraySyn burner and applied flowrates in this work.

Stream	D_in/mm	D_out/mm	Flowrate
Liquid	0.0	0.40	2 mL/min
Dispersion	0.75	1.50	10 slm
Pilot	6.0	15.0	18 slm
Co-flow	15.0	70.0	120 slm

2. Experimental configuration and data

2.1. Burner setup

In this work, the SpraySyn burner [27], which is a standardized laboratory burner for researching flame spray synthesis, is considered. The burner configuration is illustrated in Fig. 1. The SpraySyn flame is a turbulent piloted spray flame and consists of four concentrically arranged streams. The liquid precursor-solvent mixture in the center is atomized by a high-momentum coaxial oxygen stream. The spray flame is stabilized by the exhaust gases from a flat burner-stabilized laminar pilot flame. To shield the flame from the environment and to facilitate nanoparticle transport, a co-flow is applied. LES are performed for the standard operating conditions with two different liquid precursor-solvent mixtures. For validation, an LES is performed with pure ethanol as liquid fuel without any precursor since, for this case, more experimental results are available in the literature than for the targeted synthesis case. The synthesis case uses ethanol as the solvent with 0.05 mol/L iron(III) nitrate nonahydrate as the precursor. 2 ml/min of the precursor-solvent mixture are atomized by 10 slm of oxygen. The pilot flame is operated with a mixture of oxygen and methane at an equivalence ratio of 0.25. The flow rate of the mixture is 18 slm. 120 slm of nitrogen are applied as co-flow. The burner dimensions and flow rates are summarized in Table 1.

2.2. Particle measurements

As part of this work, experiments were performed to further extend the data from the work of Sellmann et al. [24] for the considered synthesis case. The particle size distribution was measured in situ using a Hole In A Tube (HIAT) probing system, which was coupled to a Scanning Mobility Particle Sizing (SMPS) device. The tube has an outer diameter of 10 mm and crosses the entire flame horizontally. The sampling hole's diameter measures 1 mm. The SMPS device is from TSI

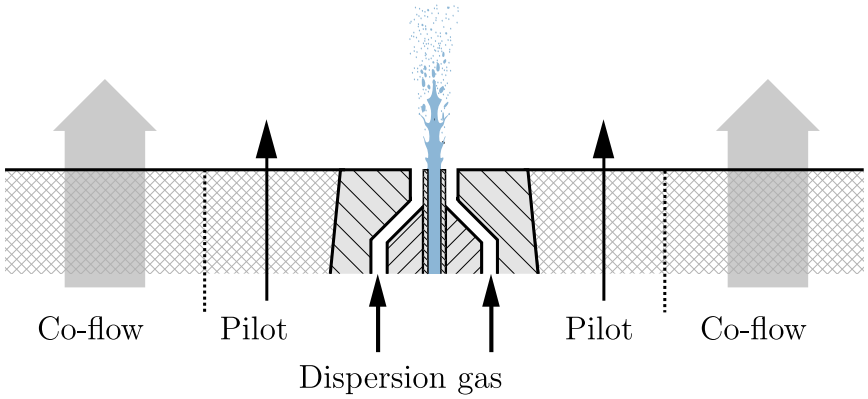

Fig. 1. Schematic illustration of the SpraySyn burner.

Incorporated and has a lower detection limit of 1 nm. Particle size distributions were measured at different heights above the burner along the centerline. For each height, quenching experiments were performed, in which the dilution flow rate through the pipe is successively increased. With increasing dilution flow rate, the particle properties converge to a final value. In that range of converged particle properties, reliable particle data can be obtained. Additionally, three measurements were performed for each dilution ratio of the quenching experiment. For a detailed description of the experimental setup and procedure, the reader is referred to the work of Tischendorf et al. [35].

3. Model formulation

In this section, the used model formulation, including the customized sub-models, will be explained. The overall model for spray flame synthesis can be divided into three parts, where each part focuses on modeling one of the phases present in the process: gas, liquid, and solid. The coupling between the phases is described in the corresponding subsection.

3.1. Gas phase modeling

The LES approach with a flamelet model is used for describing the turbulent reacting gas phase. In that approach, the flow is modeled using the Favre-filtered variable density Navier–Stokes equations, which read

$$\frac{\partial \bar{\rho}}{\partial t} + \nabla \cdot (\bar{\rho}\widetilde{\mathbf{u}}) = \Gamma_\rho \tag{1}$$

$$\frac{\partial \bar{\rho}\widetilde{\mathbf{u}}}{\partial t} + \nabla \cdot (\bar{\rho}\widetilde{\mathbf{u}}\widetilde{\mathbf{u}}) = -\nabla \bar{p} + \nabla \cdot (\bar{\boldsymbol{\sigma}} + \boldsymbol{\sigma}_{SF}) + \boldsymbol{\Gamma}_{\rho u}. \tag{2}$$

Here, ρ is the density, $\mathbf{u}$ the velocity tensor, p the pressure, $\boldsymbol{\sigma}$ the stress-tensor, and $\boldsymbol{\sigma}_{SF}$ the subfilter stress tensor. Overline denotes spatial filtering, the tilde Favre-filtering. The coupling with the liquid phase is realized using volumetric source terms for mass, Γ_ρ, and momentum, $\boldsymbol{\Gamma}_{\rho u}$. The effects of the transition from gas to solid on mass and momentum are neglected due to their small amounts. The gas phase is considered as a Newtonian fluid, and the subfilter stress tensor is closed using a dynamic Smagorinsky model with Lagrangian averaging [36,37].

Modeling spray combustion is complex due to its multi-regime nature and a subject of ongoing research. Non-Premixed Flamelet Progress Variable (NP-FPV) models provide a practical approach and are known to perform well in lean conditions [38]. Hence, the NP-FPV model is adopted in this work. However, the classical NP-FPV model applied to the SpraySyn burner suffers from an inaccurate description of the pilot flame stream as it is defined for two streams [39]. In particular, the contribution of the residual oxygen present from the lean pilot flame cannot be properly modeled. To overcome this model inaccuracy, a three-stream formulation based on a previously proposed model for MILD combustion [40] is adapted in this work.

The additional degree of freedom imposed by the pilot exhaust requires a second mixture fraction to be able to describe the local mixture state. In contrast to the three-stream combustion model proposed by Ihme and See [40], which uses a mixture fraction definition based on elementary mass fractions, a general definition according to

$$Z_\alpha = \frac{\dot{m}_\alpha}{\dot{m}_0 + \dot{m}_1 + \dot{m}_2} \tag{3}$$

is used in this work. Here, indices 1 and 2 refer to the fuel and the pilot stream, respectively. The index 0 describes both, the dispersion gas and the co-flow. The latter is modeled such that its composition equals that of the dispersion gas, and no additional mixture fraction is required. Since the sum of the two mixture fractions is constrained by unity, the resulting domain of the mixture state is defined by a unit triangle. To describe combustion in this triangular mixture fraction space, Hasse and Peters [41] derived two-dimensional flamelet equations using a two-scale asymptotic analysis. For convenience, the triangular mixture fraction space is transformed into a unit square domain using a coordinate transformation similar to Doran et al. [42]. The modified mixture fractions for the fuel and pilot stream are defined by $Z_1^* = Z_1$ and $Z_2^* = Z_2/(1-Z_1)$. Assuming steady-state and negligible gradient of scalars with respect to Z_2^*, the one-dimensional steady flamelet equation [43] describes the chemistry inside the (Z_1^*,Z_2^*)-state space. The dependence on Z_2^* is then imposed by the boundary conditions at $Z_1^* = 0$ described by scalar mixing. The solutions to the flamelet equations can be written using the flamelet progress variable approach [39] as $Y_k = Y_k(Z_1^*, Z_2^*, C)$, where Y_k is the mass fraction of species k and C is the progress variable defined by $C = Y_{\mathrm{H_2O}} + Y_{\mathrm{CO}} + Y_{\mathrm{CO_2}} + Y_{\mathrm{H_2}}$.

To apply the previously presented three-stream combustion model in an LES, a turbulence closure is also required. Turbulence closure is achieved using the presumed Filter Probability Density Function (FPDF) approach. The filtered quantities are obtained by integrating the solutions of the steady one-dimensional flamelet equation with a presumed joint FPDF. The joint FPDF can be expressed in terms of the joint FPDF of the two mixture fractions and the conditional FPDF for the progress variable. As in previous models for a single mixture fraction [39], the conditional FPDF for the progress variable is assumed to be a delta distribution. The conditional mean is given by a steady flamelet solution, which depends on both mixture fractions in the considered case. Assuming that Z_1^* and Z_2^* are independent, the marginal FPDFs for Z_1^* and Z_2^* must be modeled. This work uses a beta and delta distribution for the marginal FPDF of Z_1^* and Z_2^*, respectively. Hence, the FPDF reads

$$P(Z_1^*, Z_2^*, C) = \beta(Z_1^*; \widetilde{Z_1^*}, \widetilde{Z_1^{*\prime\prime 2}})\delta(Z_2^* - \widetilde{Z_2^*})\delta(C - \widetilde{C}), \tag{4}$$

and can be used to tabulate the filtered mass fractions according to

$$\widetilde{Y_k} = \widetilde{Y_k}(\widetilde{Z_1^*}, \widetilde{Z_1^{*\prime\prime 2}}, \widetilde{Z_2^*}, \widetilde{C}). \tag{5}$$

Here, $\widetilde{Z_1^{*\prime\prime 2}}$ is the scalar variance required as the second parameter for the beta distribution. To use the tabulation according to (5), the local values of $\widetilde{Z_1^*}$, $\widetilde{Z_1^{*\prime\prime 2}}$, $\widetilde{Z_2^*}$, and $\widetilde{C}$ are required. As the statistical independence between Z_1^* and Z_2^* implies $\widetilde{Z_2^*} = \widetilde{Z_2}/(1-\widetilde{Z_1})$ and the transport equation for $\widetilde{Z_2^*}$ includes an additional term, it is convenient to solve a transport equation for $\widetilde{Z_2}$ rather than $\widetilde{Z_2^*}$. For the filtered mixture fraction $\widetilde{Z_\alpha}$, the transport equation reads

$$\frac{\partial \bar{\rho}\widetilde{Z_\alpha}}{\partial t} + \boldsymbol{\nabla}\cdot\left(\bar{\rho}\widetilde{\mathbf{u}}\widetilde{Z_\alpha}\right) = \boldsymbol{\nabla}\cdot\left(\bar{\rho}D\boldsymbol{\nabla}\widetilde{Z_\alpha}\right) + \Gamma_Z. \tag{6}$$

Here, Γ_Z is the source term due to spray evaporation, and D is the diffusivity, which consists of molecular (D_m) and turbulent (D_t) contributions. Assuming unity Lewis numbers, the molecular diffusivities are equal for all scalars. The turbulent contribution is consistent with the eddy viscosity computed using the dynamic Smagorinsky model [36,37]. The filtered mixture fraction variance $\widetilde{Z_1^{*\prime\prime 2}}$ is obtained from the second moment of the mixture fraction $\widetilde{Z_1^{*2}}$, which is known from solving

$$\frac{\partial \bar{\rho}\widetilde{Z_1^{*2}}}{\partial t} + \boldsymbol{\nabla}\cdot\left(\bar{\rho}\widetilde{\mathbf{u}}\widetilde{Z_1^{*2}}\right) = \boldsymbol{\nabla}\cdot\left(\bar{\rho}D\boldsymbol{\nabla}\widetilde{Z_1^{*2}}\right) + \bar{\rho}\widetilde{\chi} + \Gamma_{Z^2}. \tag{7}$$

Here, Γ_{Z^2} is the source term due to spray evaporation. The unclosed filtered scalar dissipation rate $\widetilde{\chi}$ is obtained according to the model of Girimaji and Zhou [44].

In classical flamelet models, the filtered temperature is also obtained from the flamelet solutions tabulation. In spray combustion cases, however, local cooling due to droplet heating cannot be described with this approach. Instead, a transport equation for the filtered enthalpy is solved, and the local filtered temperature is iteratively obtained using the local composition and the local filtered enthalpy. The transport equations for the filtered enthalpy is

$$\frac{\partial \bar{\rho}\widetilde{H}}{\partial t} + \boldsymbol{\nabla}\cdot\left(\bar{\rho}\widetilde{\mathbf{u}}\widetilde{H}\right) = \boldsymbol{\nabla}\cdot\left(\bar{\rho}D\boldsymbol{\nabla}\widetilde{H}\right) + \Gamma_H. \tag{8}$$

Here, the source term, Γ_H, accounts for the energy exchange between the liquid and gas phases.

Because the fuel is in liquid form, the temperature at the fuel boundary must account for the energy required to evaporate it. This temperature is obtained by setting the gas phase fuel's enthalpy to the liquid fuel's enthalpy. This approach was already used in previous works [45,46], and the reader is referred to them for more details.

3.2. Liquid phase modeling

The dispersed liquid phase is modeled using a Lagrangian approach. Each spray droplet is explicitly tracked and considered a point particle. Each droplet is characterized by its position ($\mathbf{x}$), velocity ($\mathbf{u}_{\text{drop}}$), mass (m_{drop}), and temperature (T_{drop}), which are governed by a system of ordinary differential equations [47]:

$$\frac{\mathrm{d}\mathbf{x}}{\mathrm{d}t} = \mathbf{u}_{\text{drop}}, \tag{9}$$

$$\frac{\mathrm{d}\mathbf{u}_{\text{drop}}}{\mathrm{d}t} = \frac{f_1}{\tau_{\text{drop}}}(\mathbf{u}_{\text{drop}} - \widetilde{\mathbf{u}}), \tag{10}$$

$$\frac{\mathrm{d}m_{\text{drop}}}{\mathrm{d}t} = -\frac{\mathrm{Sh}}{3\mathrm{Sc_g}}\left(\frac{m_{\text{drop}}}{\tau_{\text{drop}}}\right)\ln(1+B_{\mathrm{M}}), \tag{11}$$

$$\frac{\mathrm{d}T_{\text{drop}}}{\mathrm{d}t} = \frac{\mathrm{Nu}}{3\mathrm{Pr_g}}\left(\frac{C_{\mathrm{p,g}}}{C_l}\right)\left(\frac{f_2}{\tau_{\text{drop}}}\right)(\widetilde{T} - T_{\text{drop}}) + \frac{\mathrm{d}m_{\text{drop}}}{\mathrm{d}t}\frac{L_v}{m_{\text{drop}}C_l}. \tag{12}$$

Here, f_1 is the drag coefficient, τ_{drop} is the droplet time constant, Sh is the Sherwood number, $\mathrm{Sc_g}$ is the gas phase Schmidt number, B_{M} is the Spalding transfer number, Nu is the Nusselt number, $\mathrm{Pr_g}$ is the gas phase Prandtl number, $C_{\mathrm{p,g}}$ is the isobaric heat capacity of the gas phase, C_l is the heat capacity of the liquid, f_2 is a correction to heat transfer due to evaporation, and L_v is the heat of vaporization. The definition of these quantities follows model M1 with a definition of f_2 according to model M7, described by Miller et al. [47]. The model is not extended to account for complex phenomena such as micro-explosions, liquid phase reactions, and precipitation, which can take place in spray flame synthesis, as mentioned in Section 1.

The spray source terms for mass, momentum, mixture fraction, and enthalpy are given by

$$\Gamma_\rho = \Gamma_Z = \frac{1}{V_\Delta}\sum_d\left(-\frac{\mathrm{d}m_{\text{drop}}}{\mathrm{d}t}\right), \tag{13}$$

$$\boldsymbol{\Gamma}_{\rho u} = \frac{1}{V_\Delta}\sum_d\left(-\mathbf{u}_{\text{drop}}\frac{\mathrm{d}m_{\text{drop}}}{\mathrm{d}t} - m_{\text{drop}}\frac{\mathrm{d}\mathbf{u}_{\text{drop}}}{\mathrm{d}t}\right), \tag{14}$$

$$\Gamma_{Z^2} = \frac{1}{V_\Delta}\sum_d\left(-\frac{\mathrm{d}m_{\text{drop}}}{\mathrm{d}t}\right), \tag{15}$$

$$\Gamma_H = \frac{1}{V_\Delta}\sum_d\left(-C_l m_{\text{drop}}\frac{\mathrm{d}T_{\text{drop}}}{\mathrm{d}t} + (L_v - H_{vap})\frac{\mathrm{d}m_{\text{drop}}}{\mathrm{d}t}\right). \tag{16}$$

Here, the summation index d indicates a loop over all drops within the LES mesh cell with volume V_Δ, and H_{vap} denotes the specific enthalpy of the vapor at T_{drop}. Note that the source terms are presented using a spatially first-order coupling for readability. The actual implementation, however, uses a second-order extrapolation.

3.3. Solid phase modeling

The solid nanoparticle dynamics are modeled using a bivariate method of moments. Each particle is described by its volume (V_i) and surface area (S_i), from which aggregate and primary particle quantities can be computed. The joint moments of the number density function are given by $M_{[x][y]} = \sum_{i=0}^{\infty} V_i^x S_i^y N_i$, where N_i is the number density of particle i. In the method of moments, equations for moments of the Number Density Function (NDF) are solved rather than for the NDF itself. A challenge in moment methods is that the source terms typically appear unclosed meaning that moments are required that are not directly solved. The closure approach is particularly relevant, and several approaches have been developed. One approach is HMOM, which combines the interpolative closure [48] and the direct quadrature approach [18]. HMOM provides the advantage of an inherent bimodality. As Sellmann et al. [24] reported on bimodal distributions, HMOM is considered an appropriate closure approach for this work. HMOM with first-order interpolation is used in this work. The closure approach reads

$$M_{[x][y]} = N_0 V_0^x S_0^y + N_{\mathrm{L}} V_{\mathrm{L}}^x S_{\mathrm{L}}^y, \tag{17}$$

where the subscripts 0 and L refer to the nucleus and large particle, respectively. In the first-order interpolation approach of HMOM, equations are solved for three moments ($M_{[0][0]}$,$M_{[1][0]}$, and $M_{[0][1]}$) and the number density of the nuclei N_0.

Neglecting particle diffusion, the transport equation for the filtered density-weighted moments, $m_{[x][y]} = M_{[x][y]}/\rho$, and the filtered density-weighted number density of the nuclei, $n_0 = N_0/\rho$, are given by

$$\frac{\partial \bar{\rho}\tilde{n}_0}{\partial t} + \boldsymbol{\nabla}\cdot\left(\bar{\rho}\widetilde{\mathbf{u}}\tilde{n}_0\right) = \boldsymbol{\nabla}\cdot\left(\bar{\rho}D_t\boldsymbol{\nabla}\tilde{n}_0\right) + \bar{\dot{N}}_0, \tag{18}$$

$$\frac{\partial \bar{\rho}\widetilde{m}_{[x][y]}}{\partial t} + \boldsymbol{\nabla}\cdot\left(\bar{\rho}\widetilde{\mathbf{u}}\widetilde{m}_{[x][y]}\right) = \boldsymbol{\nabla}\cdot\left(\bar{\rho}D_t\boldsymbol{\nabla}\widetilde{m}_{[x][y]}\right) + \bar{\dot{M}}_{[x][y]}. \tag{19}$$

The source terms, $\bar{\dot{N}}_0$ and $\bar{\dot{M}}_{[x][y]}$, are given by the formation processes. This work considers particle inception, adsorption, coagulation, and sintering. While the source terms for particle inception, adsorption, and coagulation were adapted from an existing soot model [20,49], the source term for sintering was consistently derived. Here, the unfiltered source terms are described before introducing the turbulence closure approach.

Particle inception describes the birth of particles and is linked to gas phase chemistry. In this work, the relevance of precursor chemistry is studied. For this, three different models have been tested. The first model describes a limiting case in which precursor chemistry is fast, and evaporation limits the inception rate. Similar to Sellmann et al. [24], it is assumed that a mixture of ethanol, water, oxygen, nitrogen dioxide, and iron oxide evaporates. However, instantaneous inception is assumed instead of considering iron oxide as gas phase species, which is consumed and formed again. In that case, the moment source term is directly linked to the spray source term and is given by

$$\dot{M}_{[x][y]}^{\mathrm{Inc}} = N_{\mathrm{A}} \frac{Y_{\mathrm{Fe_2O_3,liq}} \Gamma_{\rho}}{W_{\mathrm{Fe_2O_3}}} V_0^x S_0^y. \tag{20}$$

Here, N_{A} is the Avogadro constant, $Y_{\mathrm{Fe_2O_3,liq}}$ is the mass fraction of iron oxide in the liquid, and $W_{\mathrm{Fe_2O_3}}$ is the molar mass of iron oxide. Assuming instantaneous inception implies no intermediate iron species interacting with the ethanol combustion chemistry. From laminar flames, however, flame inhibition effects are known from iron species [50]. Hence, it is reasonable to include detailed iron chemistry. Moreover, the inception process might be kinetically limited. For the formation of iron oxide from iron pentacarbonyl, a reaction mechanism was developed by Wlokas et al. [51]. In that mechanism, iron pentacarbonyl is decomposed into iron and carbon monoxide and defines the initiation reaction for the iron sub-mechanism. In a sequence of reactions, iron oxide is finally formed. The formation reaction was used as the inception reaction. For the second model, it is assumed that ethanol, water, and iron nitrate evaporate. In analogy to the work of Wlokas et al. [51], iron nitrate decomposes into iron, nitrogen dioxide, and oxygen, defining the initiation for the iron sub-mechanism. Mu and Perlmutter [34] provide kinetic parameters for the global decomposition of solid iron nitrate into solid iron oxide. Using their pre-exponential factor and activation energy for the proposed gas phase reaction was found to be unusable. The reaction velocity was too fast to achieve convergence during the flamelet computations. Instead, the parameters were adapted to achieve a sufficiently fast decomposition while maintaining the reported decomposition temperature. The finally used parameters are $E = 222.196\,\mathrm{kJ/mol}$ and $B = 2.6 \times 10^{24}\,1/\mathrm{s}$. With w_{Inc} being the inception rate, the moment source term is then defined as

$$\dot{M}_{[x][y]}^{\mathrm{Inc}} = N_{\mathrm{A}}\, w_{\mathrm{Inc}} V_0^x S_0^y. \tag{21}$$

Independent of the model, the source term for N_0 is given by $\dot{N}_0 = \dot{M}_{[0][0]}^{\mathrm{Inc}}$.

As stated in Section 1, surface adsorption is an additional particle growth process with potential relevance. Therefore, the third model tested in this work adds adsorption to the second model. In analogy to works in soot [20,49] or titania formation [52], adsorption is modeled as a collision of a gas phase species and a particle. The species involved in the inception reaction is a natural choice for the collision species involved in adsorption. In this work, $Fe_2OOOH + (Fe_2O_3)_n \rightarrow (Fe_2O_3)_{n+1} + H$ is assumed as adsorption reaction. Following Mueller et al. [49], the moment source term for adsorption is given by

$$\dot{M}_{[x][y]}^{\mathrm{Ads}} = N_{\mathrm{A}} C_{\mathrm{Fe_2OOOH}} \left(\sum_{i=0}^{\infty} \beta_i^{\mathrm{Ads}} \left(x \frac{V_0}{V_i} + y \frac{\delta S}{S_i} \right) V_i^x S_i^y N_i \right), \tag{22}$$

where $C_{\mathrm{Fe_2OOOH}}$ is the concentration of Fe_2OOOH, and β_i^{Ads} is the collision frequency. As in the model of Mueller et al. [49], it is assumed that adsorption makes the particle more spherical, and the proposed power law fit for the change of surface area, δS, is used. The collision frequency is modeled using a first-order Taylor series approximation of the free-molecular collision kernel and reads

$$\beta_i^{\mathrm{Ads}} = \epsilon \sqrt{\frac{\pi k_{\mathrm{B}} N_A T}{2 W_{\mathrm{Fe_2OOOH}}}} \left(1 + \frac{1}{2} \frac{W_{\mathrm{Fe_2OOOH}}}{N_{\mathrm{A}} \rho_{\mathrm{Fe_2O_3}} V_i} \right) (d_{\mathrm{Fe_2OOOH}} + d_{\mathrm{c},i})^2. \tag{23}$$

Here, $d_{\mathrm{Fe_2OOOH}}$ and $W_{\mathrm{Fe_2OOOH}}$ denote the collision diameter and molecular mass of Fe_2OOOH, respectively. k_{B} is the Boltzmann constant. The source term for the number density of nuclei is given by

$$\dot{N}_0^{\mathrm{Ads}} = -\beta_0 C_{\mathrm{Fe_2OOOH}} N_0. \tag{24}$$

Following Mueller et al. [49], the moment source term for coagulation reads

$$\dot{M}_{[x][y]}^{\mathrm{Coag}} = \frac{1}{2} \sum_{i,j=0}^{\infty} \beta_{i,j} \left(V_{i+j}^x S_{i+j}^y - V_i^x S_i^y - V_j^x S_j^y \right) N_i N_j, \tag{25}$$

where i and j indicate the colliding particles and $i + j$ the resulting particle. Pure aggregation is considered in this work, meaning that $V_{i+j} = V_i + V_j$ and $S_{i+j} = S_i + S_j$. The coagulation source term for the number density of nuclei is given by

$$\dot{N}_0^{\mathrm{Coag}} = -\sum_{i=0}^{\infty} \beta_{0,i} N_0 N_0. \tag{26}$$

In the free molecular regime, the collision frequency, $\beta_{i,j}$, of two particles is given by

$$\beta_{i,j}^{\mathrm{fm}} = \varepsilon \sqrt{\frac{\pi k_{\mathrm{B}} T}{2 \rho_{\mathrm{Fe_2O_3}}}} \cdot \left(\frac{1}{V_i} + \frac{1}{V_j} \right)^{\frac{1}{2}} (d_{\mathrm{c},i} + d_{\mathrm{c},j})^2, \tag{27}$$

where $\rho_{\mathrm{Fe_2O_3}}$ is the density of iron oxide. As experiments revealed that mainly maghemite is formed [31], a density of $4860\,\mathrm{kg/m^3}$ is used. Following Kruis et al. [15], the collision diameter can be expressed using the fractal dimension, D_{f}, as

$$d_{\mathrm{c},i} = d_{\mathrm{p},i} n_{\mathrm{p},i}^{\frac{1}{D_{\mathrm{f}}}}. \tag{28}$$

Here, the primary particle diameter is $d_{\mathrm{p},i} = 6V_i/S_i$, and the number of primary particles is $n_{\mathrm{p},i} = 1/36 \cdot S_i^3/V_i^2$. To account for van der Waals forces between the particles, the free molecular collision frequency is enhanced using the enhancement factor ε. The enhancement factor's temperature dependency is modeled using a power law. The power law was fitted to the enhancement factor theory of Marlow [53], assuming equally sized particles for the interaction potential. The Hamaker constant for Fe_2O_3 was taken from the textbook of Friedlander [54]. The enhancement factor varies from about 3.5 at 300 K to about 2.2 at 2500 K and is similar to reported values for soot (2.2) [55] and titania (2.64) [56]. In the continuum regime, the collision frequency is given by

$$\beta_{i,j}^{\mathrm{cont}} = \frac{2 k_{\mathrm{B}} T}{3 \mu} \left(\frac{C_i}{d_{\mathrm{m},i}} + \frac{C_j}{d_{\mathrm{m},j}} \right) (d_{\mathrm{c},i} + d_{\mathrm{c},j}) \tag{29}$$

with d_m being the mobility diameter, which is assumed to be equal to the collision diameter. The Cunningham slip correction is $C_i = 1 + 1.257\mathrm{Kn}_i$, where the Knudsen number, Kn_i, is evaluated using the collision diameter as particle length scale. To account for the transition between both regimes, the harmonic average is used as proposed by Kazakov and Frenklach [57].

Sintering describes the finite rate fusion of particle aggregates towards a spherical particle. Consistently to the above-described moment source terms, the general source term for sintering was derived and is given by

$$\dot{M}_{[x][y]}^{\mathrm{Sint}} = \sum_{i=0}^{\infty} y \dot{S}_i V_i^x S_i^{y-1} N_i. \tag{30}$$

Here, $\dot{S}_i$ is the rate of surface area change of particle i. As sintering does not affect the number density, there is no source term for the number density of the nuclei. Using the linear relaxation model of Koch and Friedlander [58], it follows that

$$\dot{S}_i = -\frac{1}{\tau_i^{\mathrm{Sint}}} \left(S_i - \left(\frac{V_i}{V_0} \right)^{2/3} S_0 \right), \tag{31}$$

where τ_i^{Sint} is the characteristic sinter time. For the characteristic sinter time, the model of Rosenberger et al. [59] is used, employing the coefficients for a primary particle diameter exponent of four.

Table 2
Summary of the precursor chemistry and consumption models used.

Model acronym	Liquid phase species	Inception	Adsorption
InstInc	C_2H_5OH, H_2O, O_2, NO_2, Fe_2O_3	instantaneous	none
FiniteInc	C_2H_5OH, H_2O, $Fe(NO_3)_3$	$Fe_2OOOH+OH \rightarrow Fe_2O_3 + H_2O$	none
FiniteIncAds	C_2H_5OH, H_2O, $Fe(NO_3)_3$	$Fe_2OOOH+OH \rightarrow Fe_2O_3 + H_2O$	$Fe_2OOOH + (Fe_2O_3)_n \rightarrow (Fe_2O_3)_{n+1} + H$

To obtain the filtered source terms, the following consideration is essential. All moment source terms can be expressed as $\dot{M}_{[x][y]} = \sum_k f_k(\psi) g_k(\phi)$, where $f_k(\psi)$ are functions depending on the thermochemical variables ψ and $g_k(\phi)$ are functions describing products of the moment with specific exponents. Hence, a joint FPDF, including the thermochemical variables and the moments, is necessary for employing a presumed FPDF approach. In the context of soot, Mueller et al. [60] assumed statistical independence between the thermochemical variables and the moments and modeled the marginal FPDF for the moments using a double delta distribution. Note that the marginal FPDF describes the subfilter distribution of the moments and should not be confused with the particle size distribution. Recently, Berger et al. [61] showed that the double delta model is identical to a single delta model for all source terms, except coagulation, for HMOM with first-order interpolation. Moreover, Sellmann et al. [24] investigated the impact of the double delta model for their sectional model and found no significant impact. As a result, a single delta function is used as marginal FPDF for the moments in this work. Consistent to the combustion model described in Section 3.1, the same joint FPDF for the thermochemical variables is used.

While inception is essentially a gas phase process and can easily be modeled using a tabulated chemistry approach, adsorption requires modeling the interaction between the gas phase and solid phase description. One essential consequence is that no feedback from the particle phase to the thermochemical variables can be modeled. In order to not overestimate the adsorption rate, which linearly depends on the collision species concentration, a special treatment for species consumed by inception or adsorption is introduced. Similar to the works of Mueller et al. [62,63] on soot modeling, an additional transport equation for the Favre-filtered mass fraction is solved, which is given by

$$\frac{\partial \bar{\rho}\widetilde{Y}_i}{\partial t} + \boldsymbol{\nabla}\cdot\left(\bar{\rho}\widetilde{\mathbf{u}}\widetilde{Y}_i\right) = \boldsymbol{\nabla}\cdot\left(\bar{\rho}D\boldsymbol{\nabla}\widetilde{Y}_i\right) + \bar{\dot{m}}_i. \tag{32}$$

The source term for species i reads

$$\bar{\dot{m}}_i = \bar{\dot{m}}_+^{\mathrm{Tab}} + \bar{\dot{m}}_-^{\mathrm{Tab}}\left(\frac{\widetilde{Y}_i}{\widetilde{Y}_i^{\mathrm{Tab}}}\right) + \tag{33}$$

$$\nu_i^{\mathrm{Inc}} W_i \bar{\omega}_{\mathrm{Inc}}^{\mathrm{Tab}}\left(\frac{\prod_i^{N_S}\widetilde{Y}_i}{\prod_i^{N_S}\widetilde{Y}_i^{\mathrm{Tab}}}\right) + \nu_i^{\mathrm{Ads}}\frac{W_i}{W_{\mathrm{Fe_2O_3}}}\rho_{\mathrm{Fe_2O_3}}\bar{\dot{M}}_{[1][0]}^{\mathrm{Ads}}, \tag{34}$$

where W_i is the molar mass of species i, and ν_i^{Inc} and ν_i^{Ads} are the stoichiometric coefficients of species i for the inception and adsorption reaction, respectively. The first two terms in (34) represent contributions from gas-phase reactions, and the last two are from gas-phase particle interaction. Following the approach of Ihme and Pitsch [64], the gas phase contribution is split into a production ($\bar{\dot{m}}_+^{\mathrm{Tab}}$) and consumption part ($\bar{\dot{m}}_-^{\mathrm{Tab}}$). As the consumption rate depends on the species mass fraction, the rate is adjusted using the mass fraction from solving (32) and the chemistry table ($\widetilde{Y}_i^{\mathrm{Tab}}$). Similar adjustments are applied to the inception rate and to the thermochemical part of the adsorption source term. Note that a similarity assumption, as introduced by Ihme and Pitsch [64], is used in (34) to obtain a closed expression for the species mass fraction source term. To conclude the nanoparticle modeling section, the critical differences between the three models tested in this work are summarized in Table 2. In addition, acronyms are introduced, which will be used following.

Table 3
Inner (*D_in*) and outer (*D_out*) diameter of each inlet and the corresponding bulk velocity used in the performed simulations.

Stream	*D_in*/mm	*D_out*/mm	*u_bulk* m/s
Dispersion	0.75	1.50	1.324×10^2
Pilot	6.0	25.0	5.647×10^0
Co-flow	25.0	70.0	5.728×10^{-1}

4. Numerical framework and setup

The Favre-filtered governing equations are solved using the structured, finite-difference in-house low-Mach LES code CIAO [65]. Spatial derivatives are discretized using a second-order central difference scheme, except for the convective terms in scalar transport equations. Instead, a fifth-order weighted essentially non-oscillatory (WENO5) scheme [66] is used. Time integration is performed with a second-order Crank–Nicolson scheme [65]. CIAO features the Lagrangian spray model described in Section 3.2, which was successfully used in previous works in the context of engine fuel sprays [67,68]. Spray source terms are treated explicitly. The computation of the moment source terms was implemented into a library. The implementation was validated by computing the formation of titania in a premixed laminar stagnation flame and comparing the results with experimental [69,70] and numerical results [52,71]. Moment source terms are treated explicitly using a temporally averaged source term. The averaged source term is obtained by integrating the moments and involved species at a frozen thermochemical state using a high-order variable time-step integration method [72].

The computational domain is a cuboid measuring 150 mm × 55 mm × 55 mm in x, y, and z directions. The domain is non-equidistantly discretized by a mesh of 328 × 218 × 218 cells in x, y, and z directions, yielding about 15.6 million cells. The smallest cell of size $\Delta_{min} = 0.125$ mm is located at the centerline, resolving the outer diameter of the dispersion gas inlet by 12 cells. The largest cell size is located towards the exit plane with a width of $\Delta_{max} = 0.75$ mm. The domain starts right above the burner. Even though the thin annular dispersion gas gap is resolved by only 3.2 grid cells, a better performance was found than starting the domain a few millimeters above the burner, as used by Sellmann et al. [24]. The unsteady velocity field from an internal nozzle flow simulation was imposed as the boundary condition for the dispersion gas. For all other inlets, the bulk velocity is used. In order to exclude the pilot flame from the domain, an infinitely thin flame is assumed, meaning that only exhaust gases enter the domain. The composition and temperature were estimated using a burner-stabilized laminar flat flame. In contrast to a freely propagating flame, this approach includes heat losses to the burner. The outer diameter of the inlet was increased to account for the expansion. The diameter was estimated from experimental flame images. A summary of the inlet dimensions and resulting bulk velocities is given in Table 3.

In the context of Lagrangian spray models, modeling primary atomization is very challenging. For the SpraySyn burner, experimental data exist, which can be used to model the spray initialization. Shadowgraphy images [29,73] indicate that at a Height Above Burner (HAB) of about HAB = 3.5 mm primary breakup is completed. Hence, the

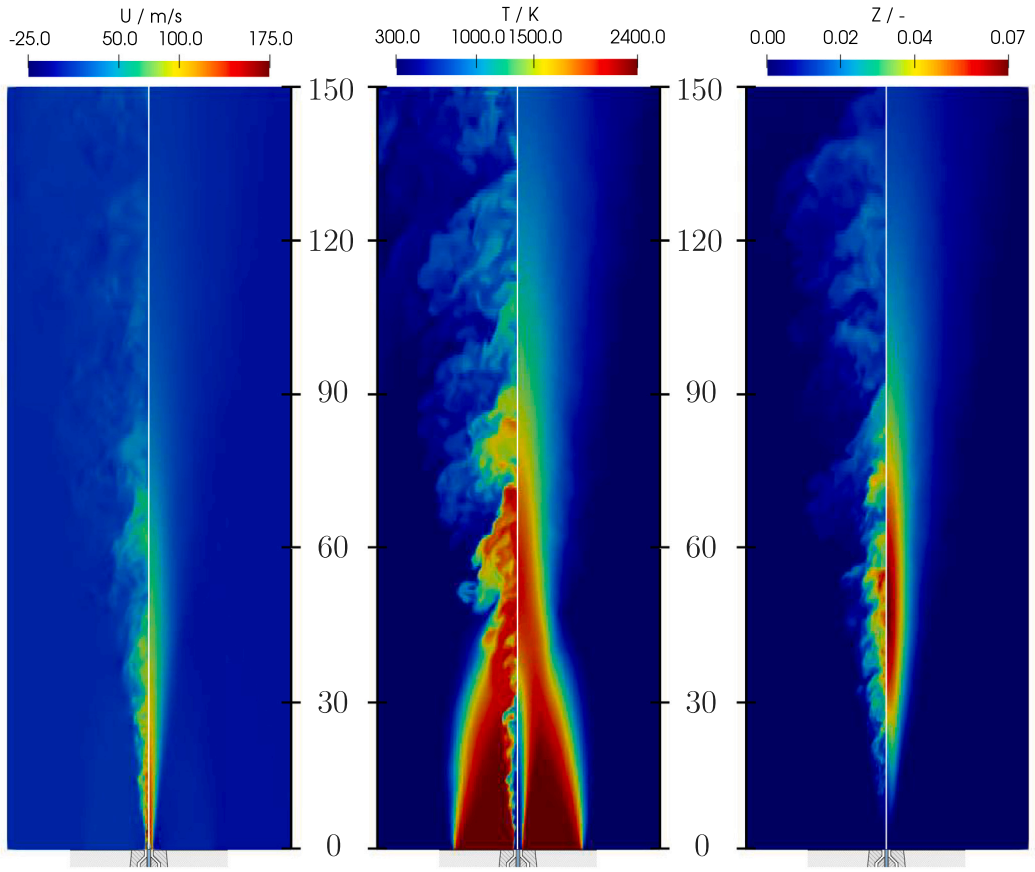

Fig. 2. Axial velocity (left), temperature (center), and fuel mixture fraction (right) on a cut plane. The left half shows an instantaneous snapshot, while the right half shows the mean field. The scales between the images provide the HAB in mm.

droplets are initialized at 3.5 mm above the burner covering the entire cross-section of a disk with a diameter of 1.5 mm. The droplet sizes are described by a log-normal distribution with a mean and Sauter-mean diameter of 12.00 µm and 17.85 µm, respectively. The droplet velocity is set to the local gas phase velocity. As the droplets still accelerate just above the burner, the velocity is reduced by 45 %. The velocity reduction factor is independent of the droplet size and hence neglects a correlation between the droplet size and velocity. A parameter study was realized to obtain the parameters for the size distribution and the velocity reduction factor. In order to exclude effects from the combustion model, the parameter study was performed using an inert spray case. The inert spray results for the final parameters are shown in Section S1 of the supplemental material.

The flamelets for the chemistry table were computed using the FlameMaster code [74]. The ethanol part of the mechanism of Cai and Pitsch [75] describes ethanol chemistry. Iron chemistry is included for Model FiniteInc and FiniteIncAds using the mechanism of Wlokas et al. [51] and the proposed decomposition reaction described in Section 3.3. Statistics are sampled over about 25 flow-through times after reaching steady-state. The flow-through time is defined using the domain length and the bulk velocity of the dispersion gas.

5. Results and discussion

5.1. Undoped flame

5.1.1. General flame shape

To visualize the general flame shape, the axial gas velocity, the temperature, and the fuel mixture fraction are shown on a cut-plane in Fig. 2. The left half always shows an instantaneous snapshot, while the right half shows the mean field. The coaxial dispersion jet is barely visible in the velocity field on the domain-length scale as it quickly merges into a conical turbulent jet. The highest negative values for the axial velocity appear just above the burner, where a small recirculation zone is present. Up to an HAB of about 20 mm, the jet core is essentially cold. Due to mixing with the exhaust gases of the laminar pilot flame and the heat release of ethanol combustion, the temperature rises in the center of the jet. At an HAB of about 30 mm, the pilot flame is fully entrained and the turbulent jet mixes with the cold co-flow. The fuel mixture fraction increases in downstream direction due to spray evaporation, and the mean mixture fraction reaches its peak at an HAB of about 45 mm. Even though droplets are still present further downstream, the fuel mixture fraction decreases as turbulent transport dominates the mixture fraction evolution.

5.1.2. Validation

After describing the overall flame shape, which remains unchanged if the precursor is added, the simulation results are compared with experimental data for validation. Here, the focus is on the droplet phase and the gas phase velocity.

The Sauter mean diameter (SMD)(left) and the axial droplet velocity (right) along the centerline are shown in Fig. 3. The simulation results are compared to three different data sets from different groups [29,76, 77]. Even though all measurements used Phase Doppler Anemometry measurement devices, substantial differences can be observed for the different experimental data sets. As this work focuses on modeling, a detailed discussion is omitted and the differences are considered as experimental uncertainty. In this context, it is worth mentioning that the measurements of Schneider et al. [77] are from the same research group that also provided measurements for the inert spray considered here. The simulation predicts a more or less constant SMD along the centerline, which is consistent with the measurements of Schneider

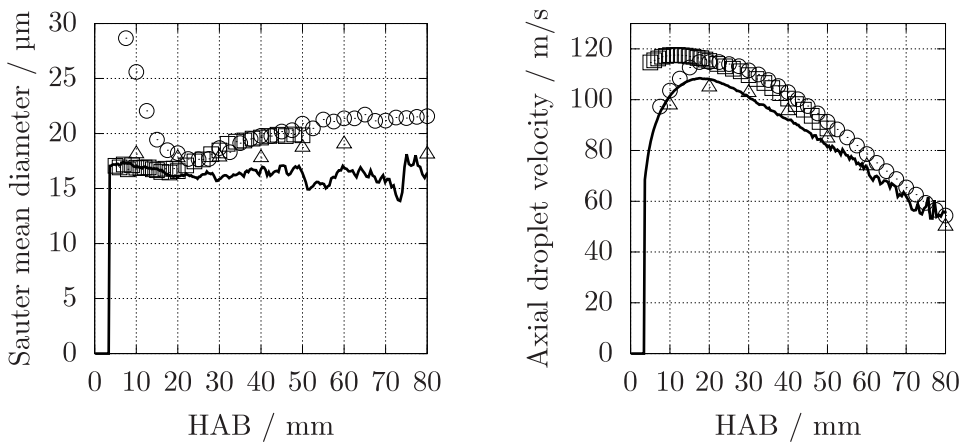

Fig. 3. Sauter mean diameter (left) and mean axial droplet velocity (right) along the centerline. The lines show the simulation results, and the symbols are the experimental data (○ [29], □ [76], △ [77]).

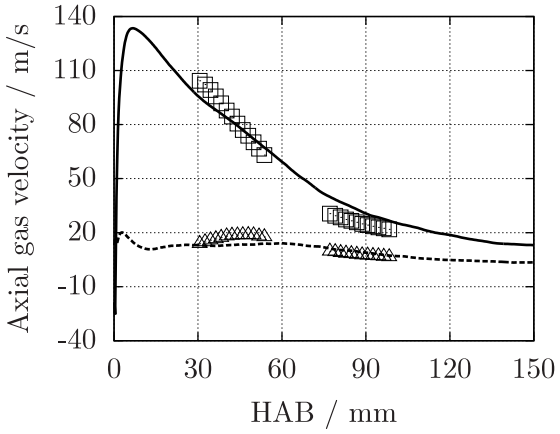

Fig. 4. Evolution along the centerline of the computed mean (—) and RMS (...) axial gas velocity compared to the experimental data of Martins et al. [78]. Squares (□) and triangles (△) correspond to the experimental mean and RMS values, respectively.

et al. [77] even though they measured slightly larger values. This is, however, different from the increase of the SMD from an HAB of 20 mm as measured by Stodt et al. [29] and Karaminejad et al. [76]. The droplet velocity increases from the initialization position up to 110 m/s at an HAB of about 17 mm. The prediction agrees very well with the data from Schneider et al. [77] and reasonably well with the other data sets further downstream.

For validating the gas phase velocity, the mean and Root Mean Square (RMS) axial gas velocities along the centerline are compared to the measurements of Martins et al. [78] in Fig. 4. Reasonably well agreement can be observed. The mean velocity appears to be underpredicted up to an HAB of about 50 mm. The mean velocity is overpredicted from this HAB, while differences seem to reduce with increasing HAB. Similarly, the axial RMS velocity is underpredicted in the region of an HAB from 30 mm to 55 mm and slightly overpredicted in the region from 75 mm HAB to 100 mm HAB. The underprediction in the first region, which is strongly governed by chemical reactions, might be related to the flame instabilities described in the works of Bieber et al. [73] and Karaminejad et al. [76]. To summarize, the LES can predict the droplet and gas phase velocity reasonably well. Additional results are shown in Subsection S2.1 of the supplementary material to support this validation.

5.2. Doped flame

5.2.1. Particle inception and precursor consumption

In this work, two particle inception models and, in addition, the effect of adsorption are studied. These particle formation processes are the only ones that impact the particle volume fraction. The particle volume fraction on a cut plane is shown for the three models in Fig. 5. The left half of each image shows an instantaneous snapshot, while the right shows the mean field. Substantial differences are observable between the three models. In particular, including detailed iron chemistry shows a strong impact. Model InstInc shows significantly larger volume fractions. As expected, the highest values are in the region between an HAB of 30 mm and 60 mm, where most of the liquid solvent-precursor mixture evaporates. In contrast, the volume fraction increases gradually with increasing HAB for model FiniteInc, which uses a finite inception rate. A similar trend is observed for model FiniteIncAds, where, because of adsorption, slightly higher values are observed. This is expected, as adsorption is an additional particle growth process. The differences between model FiniteInc and model FiniteIncAds are, however, small and are particularly present further downstream and at the outer regions of the jet, where also the highest values are present.

The right panels of Fig. 5 additionally show that a longer sampling time would be needed to converge statistics in the outer regions. Hence, for more quantitative comparisons of particle quantities, the focus is on the centerline evolution in the following. The mean particle volume fraction along the centerline is shown on the left of Fig. 6, confirming the description above. Interestingly, adsorption has essentially no impact in the flame region (25 mm < HAB < 60 mm). To investigate this further, the right panel of Fig. 6 shows the source term for the volume fraction. Note that the source term for model InstInc is scaled by a factor of 1/10. For model FiniteIncAds, the total volume fraction source term (green dotted line) and the contribution from adsorption (black solid line with squares) are shown. This reveals that adsorption has a relevant contribution to the total source term. However, the total source term shows only marginal differences from that of model FiniteInc. From this, it follows that the precursor conversion is limited by the availability of Fe_2OOOH. Interestingly, the volume fraction source term for the models with detailed iron chemistry does not converge to zero, as Fe_2OOOH is still formed and converted into iron oxide particles. This also explains the higher volume fraction values in the outer region of the jet for models FiniteInc and FiniteIncAds. As the residence time is larger than at the center of the jet, more Fe_2OOOH can be formed and is then converted into particles. From an HAB greater than 90 mm, it can be observed that adsorption dominates the source term for model FiniteIncAds. To support this discussion, the volume fraction source term on a cut plane is provided in Subsection

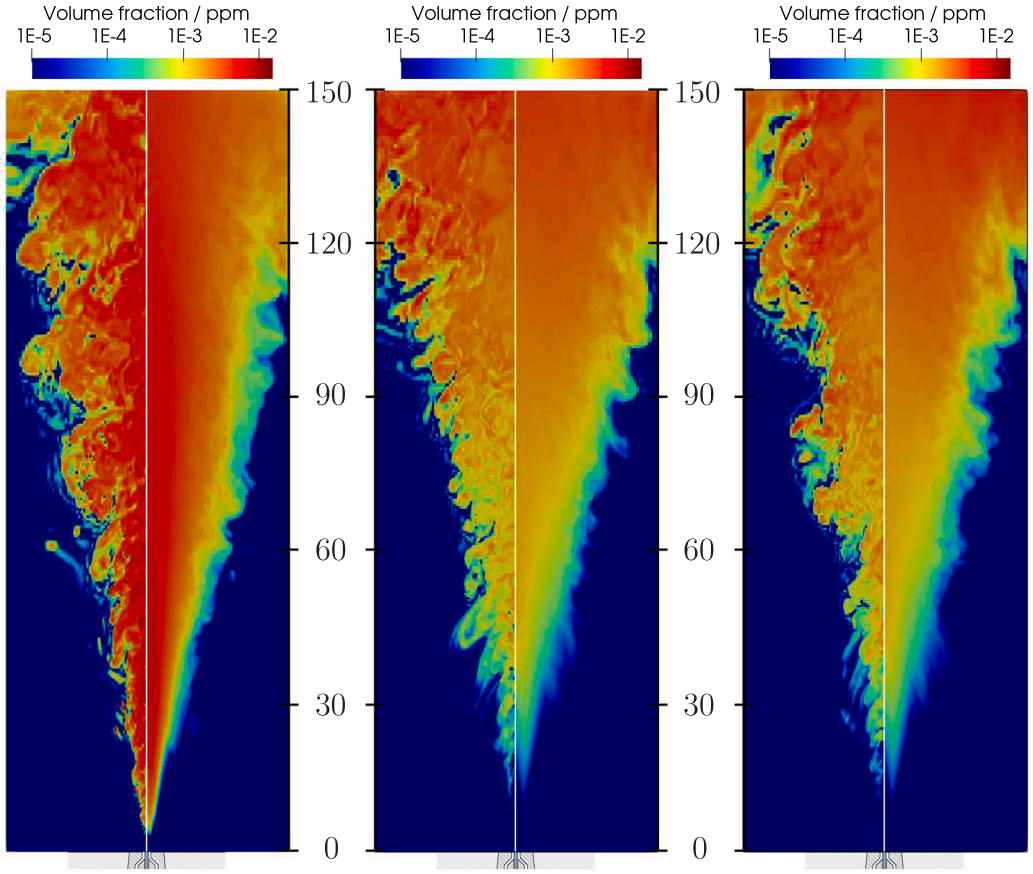

Fig. 5. Particle volume fraction on a cut plane for model InstInc (left), model FiniteInc (center), and model FiniteIncAds (right). The left half shows an instantaneous snapshot, while the right half shows the mean field. The scales between the images provide the HAB in mm.

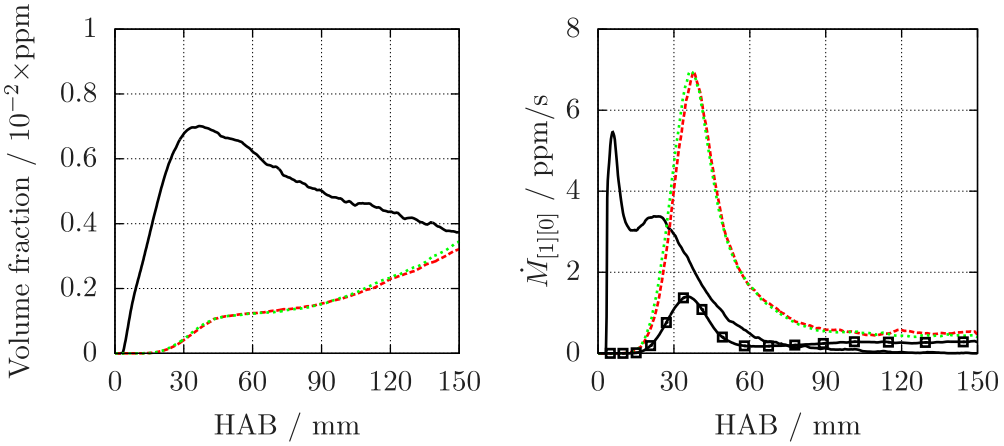

Fig. 6. Evolution along the centerline of the volume fraction (left) and the total volume fraction source term (right) comparing the three models (—— model InstInc, - - - model FiniteInc, ---- model FiniteIncAds). The solid line with squares (—□—) in the right plot shows the source term contribution of adsorption in the model FiniteIncAds. Note that the source term for model InstInc was scaled by a factor of 1/10.

S2.2 of the supplementary material. To summarize, a strong impact of using detailed iron chemistry was found compared to the assumption of instantaneous inception leading to substantial differences in the evolution of the volume fraction. Unfortunately, no experimental volume fraction data are available, which would be very helpful in assessing the inception and precursor consumption models.

5.2.2. Formation of particle aggregates

Next, the formation of particle aggregates will be discussed in the context of the tested models. Particle size distribution measurements were reported in the work of Sellmann et al. [24], and additional measurements were performed as part of this work. In Fig. 7, the simulated axial evolution of the mean volume-based diameter and the mean mobility diameter of the large particles is shown with the experimental data from Sellmann et al. [24] and from the present work. It is only focused on the large particles as the nucleus size falls below the detection limit of the measurement devices. Sellmann et al. [24] measured the particle sizes using mass spectrometry, where the size is represented the best with the volume-based diameter. In contrast, the measurements performed here used an SMPS device, which can be compared best with

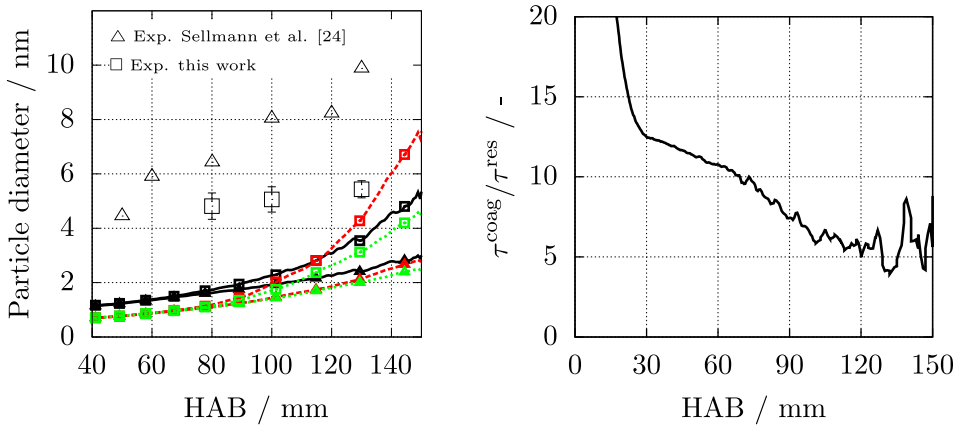

Fig. 7. Left: Evolution along the centerline of the mean particle diameter of the large particles for the three models (—— model InstInc, - - - model FiniteInc, - - - model FiniteIncAds). The lines with triangles correspond to the volume-based diameter and should be compared with the triangle symbols (△), which are the experimental data of Sellmann et al. [24]. The lines with squares show the mobility diameter and should be compared to the square symbols (□), which are the experimental data from this work. Right: Evolution along the centerline of the ratio of the characteristic coagulation time to the local residence time for model InstInc.

the mobility diameter. Hence, both diameter definitions are provided in Fig. 7. The error bars for the measurements of this work indicate the sample standard deviation and are a measure of the uncertainty. Both experimental datasets show a linear growth of the mean particle diameter. However, the growth rates differ significantly. The data from Sellmann et al. [24] increase from 4.5 nm at a HAB of 50 mm to 9.9 nm at an HAB of 130 mm. In contrast, the measurements performed in this work increase from 4.8 nm at a HAB of 80 mm to 5.4 nm at an HAB of 130 mm. In this context, it is important to mention that both measurements used probing systems, which have a dimension in the order of cm. Hence, the measurements are quite intrusive and differences can be expected. The simulation performed with model InstInc shows a linear growth for the volume-based diameter. However, it underpredicts the size by a factor of roughly 5. In contrast, the volume-based diameter for models FiniteInc and FiniteIncAds is initially smaller, however, it reaches almost the same final value due to a super-linear growth. The persistent inception most likely causes the superlinear growth and adsorption in model FiniteIncAds as already discussed in Section 5.2.1. The collision diameter follows the volume-based diameter up to an HAB of about 70 mm for all three simulations. From that on, superlinear growth is observed. This indicates that sintering slows down and that fractal aggregates are formed. The steepest increase is observed for model FiniteIncAds, while model InstInc and model FiniteInc converge to the same final value, which is close to a linear extrapolated value for the measurements of this work. The details leading to the described behaviors will be discussed in the context of the primary particle formation in Section 5.2.3.

The differences between the measurements and simulations are remarkable and need further discussion. Even for model InstInc, which assumes instantaneous inception and implies a perfect conversion rate of the precursor, the particle diameters are too small. Additionally, it was found that adsorption does not significantly impact the initial growth of the particles. Hence, it is unlikely that the particle inception and precursor consumption model is the primary source for the deviations. The remaining particle growth mechanism is coagulation. To investigate this further, the ratio of the characteristic coagulation time ($\tau^{coag} = M_{[0][0]}/\dot{M}_{[0][0]}$) to the local residence time ($\tau^{res} = \Delta x/u$), where Δx is the local axial grid spacing, is shown for model InstInc in the right of Fig. 7. From this, it becomes clear that significantly larger coagulation rates (factor 10) are needed to form particles in the order 4 nm at HAB values around 50 mm. In this context, it is interesting to mention that Sellman et al. [24] predict significantly larger particle diameters, which are already at those HAB values in the order of the experimental data. Here, it must be mentioned that the mean diameter shown by Sellmann et al. [24] is computed based on the mean particle volume, which overestimated the mean diameter. However, this should not explain the larger diameter. An essential difference to the work of Sellmann et al. [24] is the usage of a sectional model instead of HMOM, which is expected to have higher accuracy for modeling the coagulation process. Due to the much larger required coagulation rates, the closure approach is unlikely to be the primary source for the deviations. This is supported by the work of Kelesidis and Kholghy [16], who derived an enhancement factor for the monodisperse coagulation frequency of 82 % to account for polydispersity from discrete element method simulations. In addition to the moment closure, it can be expected that suitable turbulence closure models improve the comparison with the experiments. This is, for example, supported by the works of Cifuentes et al. [79] and Berger et al. [61]. Both found that coagulation rates are underestimated if a single delta model is used. It is, however, important to note that these studies focus on *a-priori* analyses, excluding the interaction of the model with numerical errors present in small-scale quantities of an LES.

To summarize the discussion, the remarkable differences between simulations and the measurements are consistent with the literature and not unexpected considering the discussed potential uncertainties. Further research is undoubtedly required to identify additional uncertainties and quantify them in experiments and models to eliminate the observed deviations. This, however, requires specialized numerical and experimental setups and, hence, is left for future work.

5.2.3. Formation of primary particles

As the model provides insights into the primary particle growth, the impact of the reaction model is briefly discussed next. The axial evolution of the mean number of primary particles (left) and the mean primary particle diameter (right) are shown for the three models in Fig. 8. In addition to the mean of the entire population, the values of the large particles are presented. Note that close to the burner, no meaningful large particle exists, leading to unreasonably high values for the number of primary particles and the primary particle diameter. From the mean number of primary particles, it can be concluded that independent of the model, sintering dominates up to an HAB of about 70 mm, and the particles are perfect spheres. Further downstream, where the temperature decreases, the mean number of primary particles increases superlinearly. The steepest increase can be observed for model FiniteInc. This is related to persistent inception, which continuously provides nuclei, which then stick to the larger particles. In contrast, in model FiniteInc, the number increases less intensely as the precursor is consumed via adsorption, which makes the particles more spherical. The mean primary particle diameter increases first

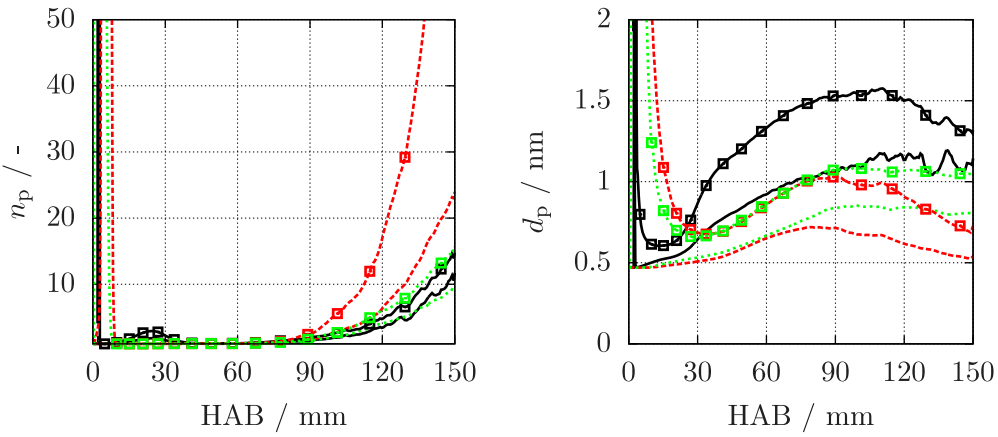

Fig. 8. Evolution along the centerline of the mean number of primary particles n_p (left) and the mean primary particle diameter d_p(right) comparing the three models (—— model InstInc, - - - model FiniteInc, - - - model FiniteIncAds). The lines with the symbols correspond to the values for the larger particles.

and decreases again further downstream. This seems to be counter-intuitive. However, it can be explained by the fact that a relevant amount of nuclei still exists up to an HAB of 150 mm, which coagulate with the large particles and do not sinter. In Subsection S2.2 of the supplementary material, the axial evolution of the mean ratio of the number density of small to large particles is provided to support this description.

6. Conclusions

This work simulated the formation of iron oxide nanoparticles in a turbulent spray flame using a comprehensive LES model, including customized submodels. The following conclusions can be drawn:

- The adapted turbulent combustion models, adequate for the considered piloted spray flame, shows sufficient validation for the liquid phase and the gas phase velocity.
- An evaporation-limited precursor chemistry model was compared to a model including detailed iron chemistry. A strong impact of the detailed iron chemistry on the volume fraction field was found. Detailed iron chemistry leads to persistent particle inception, which results in highly fractal particles with very small mean primary particle diameters.
- The effect of adsorption was studied using a third model based on the model with detailed iron chemistry. The total precursor conversion is only marginally affected by adsorption. This shows that the precursor consumption is limited by the formation of the iron species involved in the inception and adsorption reaction (Fe_2OOOH). Relatively, however, adsorption plays a significant role, leading to a smaller number of primary particles and larger mean primary particle diameters. The final particle values are comparable with the model assuming instantaneous inception.
- The mean aggregate particle diameter was compared to experimental data from Sellmann et al. [24] and with data measured within this work. Significant deviations between experiments and simulations were found independent of the precursor chemistry and consumption model. A discussion suggests that a combination of different uncertainties within the experiments and simulation leads to the observed deviations. This includes the spray measurements, the experimental probing system, the moment closure approach, moment turbulence closure, the gas phase description, and the role of unsteady effects like flame instabilities.

Future experimental and numerical work is necessary to clarify these deviations and obtain a reliable model. The findings of this work serve as a step forward towards this goal.

Declaration of competing interest

The authors declare the following financial interests/personal relationships which may be considered as potential competing interests: The authors declare that they have no known competing financial interests or personal relationships that could have appeared to influence the work reported in this paper.

Data availability

Data will be made available on request.

Acknowledgments

This work was supported by the Deutsche Forschungsgemeinschaft (DFG, German Research Foundation) through SPP1980 (Project number 375857587) and by the European Union's Horizon 2020 research and innovation program under the Center of Excellence in Combustion (CoEC) project (Grant agreement number 952181). Computing time was provided at the NHR Center NHR4CES at RWTH Aachen University (Project number p0020069).

Appendix A. Supplementary data

Supplementary material related to this article can be found online at https://doi.org/10.1016/j.jaecs.2023.100191.

References

[1] Teoh WY, Amal R, Mädler L. Flame spray pyrolysis: An enabling technology for nanoparticles design and fabrication. Nanoscale 2010;2:1324. http://dx.doi.org/10.1039/c0nr00017e.
[2] Gul S, Khan SB, Rehman IU, Khan MA, Khan MI. A comprehensive review of magnetic nanomaterials modern day theranostics. Front Mater 2019;6. http://dx.doi.org/10.3389/fmats.2019.00179.
[3] Gupta AK, Gupta M. Synthesis and surface engineering of iron oxide nanoparticles for biomedical applications. Biomaterials 2005;26:3995–4021. http://dx.doi.org/10.1016/j.biomaterials.2004.10.012.
[4] Huber D. Synthesis, properties, and applications of iron nanoparticles. Small 2005;1:482–501. http://dx.doi.org/10.1002/smll.200500006.
[5] Majewski P, Thierry B. Functionalized magnetite nanoparticles—Synthesis, properties, and bio-applications. Crit Rev Solid State Mater Sci 2007;32:203–15. http://dx.doi.org/10.1080/10408430701776680.
[6] Pankhurst QA, Connolly J, Jones SK, Dobson J. Applications of magnetic nanoparticles in biomedicine. J Phys D: Appl Phys 2003;36:R167. http://dx.doi.org/10.1088/0022-3727/36/13/201.
[7] Sodipo BK, Aziz AA. Recent advances in synthesis and surface modification of superparamagnetic iron oxide nanoparticles with silica. J Magn Magn Mater 2016;416:275–91. http://dx.doi.org/10.1016/j.jmmm.2016.05.019.

[8] Strobel R, Pratsinis SE. Flame aerosol synthesis of smart nanostructured materials. J Mater Chem 2007;17:4743–56. http://dx.doi.org/10.1039/b711652g.

[9] Li S, Ren Y, Biswas P, Tse SD. Flame aerosol synthesis of nanostructured materials and functional devices: Processing, modeling, and diagnostics. Prog Energy Combust Sci 2016;55:1–59. http://dx.doi.org/10.1016/j.pecs.2016.04.002.

[10] Gröhn AJ, Pratsinis SE, Wegner K. Fluid-particle dynamics during combustion spray aerosol synthesis of ZrO 2. Chem Eng J 2012;191:491–502. http://dx.doi.org/10.1016/j.cej.2012.02.093.

[11] Weise C, Menser J, Kaiser SA, Kempf A, Wlokas I. Numerical investigation of the process steps in a spray flame reactor for nanoparticle synthesis. Proc Combust Inst 2015;35:2259–66. http://dx.doi.org/10.1016/j.proci.2014.05.037.

[12] Meierhofer F, Mädler L, Fritsching U. Nanoparticle evolution in flame spray pyrolysis—Process design via experimental and computational analysis. AIChE J 2020;66:e16885. http://dx.doi.org/10.1002/aic.16885.

[13] Torabmostaedi H, Zhang T, Foot P, Dembele S, Fernandez C. Process control for the synthesis of ZrO2 nanoparticles using FSP at high production rate. Powder Technol 2013;246:419–33. http://dx.doi.org/10.1016/j.powtec.2013.05.006.

[14] Torabmostaedi H, Zhang T. Numerical simulation of TiO2 nanoparticle synthesis by flame spray pyrolysis. Powder Technol 2018;329:426–33. http://dx.doi.org/10.1016/j.powtec.2018.01.051.

[15] Kruis FE, Kusters KA, Pratsinis SE, Scarlett B. A simple model for the evolution of the characteristics of aggregate particles undergoing coagulation and sintering. Aerosol Sci Technol 1993;19:514–26. http://dx.doi.org/10.1080/02786829308959656.

[16] Kelesidis GA, Kholghy MR. A monodisperse population balance model for nanoparticle agglomeration in the transition regime. Materials 2021;14:3882. http://dx.doi.org/10.3390/ma14143882.

[17] Spicer PT, Chaoul O, Tsantilis S, Pratsinis SE. Titania formation by TiCl4 gas phase oxidation, surface growth and coagulation. J Aerosol Sci 2002;33:17–34. http://dx.doi.org/10.1016/S0021-8502(01)00069-6.

[18] Marchisio DL, Fox RO. Solution of population balance equations using the direct quadrature method of moments. J Aerosol Sci 2005;36:43–73. http://dx.doi.org/10.1016/j.jaerosci.2004.07.009.

[19] Neto PB, Meierhofer F, Meier HF, Fritsching U, Noriler D. Modelling polydisperse nanoparticle size distributions as produced via flame spray pyrolysis. Powder Technol 2020;370:116–28. http://dx.doi.org/10.1016/j.powtec.2020.05.019.

[20] Mueller ME, Blanquart G, Pitsch H. Hybrid method of moments for modeling soot formation and growth. Combust Flame 2009;156:1143–55. http://dx.doi.org/10.1016/j.combustflame.2009.01.025.

[21] Dasgupta D, Pal P, Torelli R, Som S, Paulson N, Libera J, et al. Computational fluid dynamics modeling and analysis of silica nanoparticle synthesis in a flame spray pyrolysis reactor. Combust Flame 2022;236:111789. http://dx.doi.org/10.1016/j.combustflame.2021.111789.

[22] Rittler A, Deng L, Wlokas I, Kempf A. Large eddy simulations of nanoparticle synthesis from flame spray pyrolysis. Proc Combust Inst 2017;36:1077–87. http://dx.doi.org/10.1016/j.proci.2016.08.005.

[23] Wollny P, Angel S, Wiggers H, Kempf AM, Wlokas I. Multiscale simulation of the formation of platinum-particles on alumina nanoparticles in a spray flame experiment. Fluids 2020;5:21. http://dx.doi.org/10.3390/fluids5040201.

[24] Sellmann J, Wollny P, Baik SJ, Suleiman S, Schneider F, Schulz C, et al. LES of nanoparticle synthesis in the spraysyn burner: A comparison against experiments. Powder Technol 2022;404:117466. http://dx.doi.org/10.1016/j.powtec.2022.117466.

[25] Kirchmann J, Martins FJ, Kronenburg A, Kumar A, Beyrau F. Investigation of elastic light scattering in flame spray pyrolysis modelled by a stochastic particle approach. Proc Combust Inst 2022. http://dx.doi.org/10.1016/j.proci.2022.10.018.

[26] Pratsinis SE. Flame aerosol synthesis of ceramic powders. Prog Energy Combust Sci 1998;24:197–219. http://dx.doi.org/10.1016/S0360-1285(97)00028-2.

[27] Schneider F, Suleiman S, Menser J, Borukhovich E, Wlokas I, Kempf A, et al. SpraySyn—A standardized burner configuration for nanoparticle synthesis in spray flames. Rev Sci Instrum 2019;90:085108. http://dx.doi.org/10.1063/1.5090232.

[28] Stodt MF, Gonchikzhapov M, Kasper T, Fritsching U, Kiefer J. Chemistry of iron nitrate-based precursor solutions for spray-flame synthesis. Phys Chem Chem Phys 2019;21:24793–801. http://dx.doi.org/10.1039/c9cp05007h.

[29] Stodt MFB, Kiefer J, Fritsching U. Drop dynamics in heterogeneous spray flames for nanoparticle synthesis. At Sprays 2020;30:779–97. http://dx.doi.org/10.1615/AtomizSpr.2020034819.

[30] Jüngst N, Smallwood GJ, Kaiser SA. Visualization and image analysis of droplet puffing and micro-explosion in spray-flame synthesis of iron oxide nanoparticles. Exp Fluids 2022;63:60. http://dx.doi.org/10.1007/s00348-022-03411-y.

[31] Tischendorf R, Simmler M, Weinberger C, Bieber M, Reddemann M, Fröde F, et al. Examination of the evolution of iron oxide nanoparticles in flame spray pyrolysis by tailored in situ particle sampling techniques. J Aerosol Sci 2020;154:105722. http://dx.doi.org/10.1016/j.jaerosci.2020.105722.

[32] Narasu P, Keller A, Kohns M, Hasse H, Gutheil E. Numerical study of the evaporation and thermal decomposition of a single iron(III) nitrate nonahydrate/ethanol droplet. Int J Therm Sci 2021;170:107133. http://dx.doi.org/10.1016/j.ijthermalsci.2021.107133.

[33] Keller A, Wlokas I, Kohns M, Hasse H. Solid-liquid equilibria in mixtures of iron(III) nitrate nonahydrate and ethanol or 1-propanol. Fluid Phase Equilib 2021;536:112987. http://dx.doi.org/10.1016/j.fluid.2021.112987.

[34] Mu J, Perlmutter D. Thermal decomposition of metal nitrates and their hydrates. Thermochim Acta 1982;56:253–60. http://dx.doi.org/10.1016/0040-6031(82)87033-0.

[35] Tischendorf R, Oleg P, Dupont S, Fröde F, Pitsch H, Kneer R, et al. Maghemite nanoparticles synthesis via SpraySyn2 and in situ particle characterization by hole in a tube sampling and scanning mobility particle sizing (HIAT-SMPS). Appl Energy Combust Sci 2023 [submitted for publication].

[36] Germano M, Piomelli U, Moin P, Cabot WH. A dynamic subgrid-scale eddy viscosity model. Phys Fluids A 1991;3:1760–5. http://dx.doi.org/10.1063/1.857955.

[37] Meneveau C, Lund TS, Cabot WH. A Lagrangian dynamic subgrid-scale model of turbulence. J Fluid Mech 1996;319:353–85. http://dx.doi.org/10.1017/S0022112096007379.

[38] Wang Q, Jaravel T, Ihme M. Assessment of spray combustion models in large-eddy simulations of a polydispersed acetone spray flame. Proc Combust Inst 2019;37:3335–44. http://dx.doi.org/10.1016/j.proci.2018.06.011.

[39] Pierce CD, Moin P. Progress-variable approach for large-eddy simulation of non-premixed turbulent combustion. J Fluid Mech 2004;504:73–97. http://dx.doi.org/10.1017/S0022112004008213.

[40] Ihme M, See YC. LES flamelet modeling of a three-stream MILD combustor: Analysis of flame sensitivity to scalar inflow conditions. Proc Combust Inst 2011;33:1309–17. http://dx.doi.org/10.1016/j.proci.2010.05.019.

[41] Hasse C, Peters N. A two mixture fraction flamelet model applied to split injections in a DI diesel engine. Proc Combust Inst 2005;30:2755–62. http://dx.doi.org/10.1016/j.proci.2004.08.166.

[42] Doran EM, Pitsch H, Cook DJ. Multi-dimensional flamelet modeling of multiple injection diesel engines. In: SAE 2012 world congress & exhibition. SAE International; 2012, http://dx.doi.org/10.4271/2012-01-0133.

[43] Peters N. Laminar diffusion flamelet models in non-premixed turbulent combustion. Prog Energy Combust Sci 1984;10:319–39. http://dx.doi.org/10.1016/0360-1285(84)90114-X.

[44] Girimaji SS, Zhou Y. Analysis and modeling of subgrid scalar mixing using numerical data. Phys Fluids 1996;8:1224–36. http://dx.doi.org/10.1063/1.868894.

[45] Baba Y, Kurose R. Analysis and flamelet modelling for spray combustion. J Fluid Mech 2008;612:45–79. http://dx.doi.org/10.1017/S0022112008002620.

[46] Knudsen E, Shashank, Pitsch H. Modeling partially premixed combustion behavior in multiphase LES. Combust Flame 2015;162:159–80. http://dx.doi.org/10.1016/j.combustflame.2014.07.013.

[47] Miller RS, Harstad K, Bellan J. Evaluation of equilibrium and non-equilibrium evaporation models for many-droplet gas-liquid flow simulations. Int J Multiph Flow 1998;24:1025–55. http://dx.doi.org/10.1016/S0301-9322(98)00028-7.

[48] Frenklach M. Method of moments with interpolative closure. Chem Eng Sci 2002;57:2229–39. http://dx.doi.org/10.1016/S0009-2509(02)00113-6.

[49] Mueller ME, Blanquart G, Pitsch H. A joint volume-surface model of soot aggregation with the method of moments. Proc Combust Inst 2009;32:785–92. http://dx.doi.org/10.1016/j.proci.2008.06.207.

[50] Rumminger M, Reinelt D, Babushok V, Linteris G. Numerical study of the inhibition of premixed and diffusion flames by iron pentacarbonyl. Combust Flame 1999;116:207–19. http://dx.doi.org/10.1016/S0010-2180(98)00033-9.

[51] Wlokas I, Faccinetto A, Tribalet B, Schulz C, Kempf A. Mechanism of iron oxide formation from iron pentacarbonyl-doped low-pressure hydrogen/oxygen flames. Int J Chem Kinet 2013;45:487–98. http://dx.doi.org/10.1002/kin.20786.

[52] Lindberg CS, Manuputty MY, Buerger P, Akroyd J, Kraft M. Numerical simulation and parametric sensitivity study of titanium dioxide particles synthesised in a stagnation flame. J Aerosol Sci 2019;138:105451. http://dx.doi.org/10.1016/j.jaerosci.2019.105451.

[53] Marlow WH. Derivation of aerosol collision rates for singular attractive contact potentials. J Chem Phys 1980;73:6284–7. http://dx.doi.org/10.1063/1.440126.

[54] Friedlander SK. Smoke, dust, and haze fundamentals of aerosol dynamics. New York: Oxford University Press; 2000.

[55] Harris SJ, Kennedy IM. The coagulation of soot particles with van der Waals forces. Combust Sci Technol 1988;59:443–54. http://dx.doi.org/10.1080/00102208808947110.

[56] Zhang Y, Li S, Yan W, Yao Q, Tse SD. Role of dipole-dipole interaction on enhancing Brownian coagulation of charge-neutral nanoparticles in the free molecular regime. J Chem Phys 2011;134:084501. http://dx.doi.org/10.1063/1.3555633.

[57] Kazakov A, Frenklach M. Dynamic modeling of soot particle coagulation and aggregation: Implementation with the method of moments and application to high-pressure laminar premixed flames. Combust Flame 1998;114(3):484–501. http://dx.doi.org/10.1016/S0010-2180(97)00322-2.

[58] Koch W, Friedlander S. The effect of particle coalescence on the surface area of a coagulating aerosol. J Colloid Interface Sci 1990;140:419–27. http://dx.doi.org/10.1016/0021-9797(90)90362-R.

[59] Rosenberger T, Skenderović I, Sellmann J, Wollny P, Levish A, Wlokas I, et al. Determining the sintering kinetics of Fe and FexOy-nanoparticles in a well-defined model flow reactor. Aerosol Sci Technol 2022;56:833–46. http://dx.doi.org/10.1080/02786826.2022.2089011.

[60] Mueller ME, Pitsch H. Large eddy simulation subfilter modeling of soot-turbulence interactions. Phys Fluids 2011;23:115104. http://dx.doi.org/10.1063/1.3657826.

[61] Berger L, Wick A, Attili A, Mueller ME, Pitsch H. Modeling subfilter soot-turbulence interactions in large eddy simulation: An a priori study. Proc Combust Inst 2021;38:2783–90. http://dx.doi.org/10.1016/j.proci.2020.06.386.

[62] Mueller ME, Pitsch H. Large eddy simulation of soot evolution in an aircraft combustor. Phys Fluids 2013;25:110812. http://dx.doi.org/10.1063/1.4819347.

[63] Mueller ME, Chan QN, Qamar NH, Dally BB, Pitsch H, Alwahabi ZT, et al. Experimental and computational study of soot evolution in a turbulent nonpremixed bluff body ethylene flame. Combust Flame 2013;160:1298–309. http://dx.doi.org/10.1016/j.combustflame.2013.02.010.

[64] Ihme M, Pitsch H. Modeling of radiation and nitric oxide formation in turbulent nonpremixed flames using a flamelet/progress variable formulation. Phys Fluids 2008;20:055110. http://dx.doi.org/10.1063/1.2911047.

[65] Desjardins O, Blanquart G, Balarac G, Pitsch H. High order conservative finite difference scheme for variable density low mach number turbulent flows. J Comput Phys 2008;227:7125–59. http://dx.doi.org/10.1016/j.jcp.2008.03.027.

[66] Jiang G-S, Shu C-W. Efficient implementation of weighted ENO schemes. J Comput Phys 1996;126:202–28. http://dx.doi.org/10.1006/jcph.1996.0130.

[67] Davidovic M, Falkenstein T, Bode M, Cai L, Kang S, Hinrichs J, et al. LES of n-dodecane spray combustion using a multiple representative interactive flamelets model. In: Angelberger C, editor. Oil Gas Sci Technol Rev d'IFP Energies nouvelles 2017;72:5. http://dx.doi.org/10.2516/ogst/2017019.

[68] Bode M, Falkenstein T, Chenadec VL, Kang S, Pitsch H, Arima T, et al. A new Euler/Lagrange approach for multiphase simulations of a multi-hole GDI injector. In: SAE 2015 world congress & exhibition. SAE International; 2015, http://dx.doi.org/10.4271/2015-01-0949.

[69] Tolmachoff ED, Abid AD, Phares DJ, Campbell CS, Wang H. Synthesis of nano-phase TiO2 crystalline films over premixed stagnation flames. Proc Combust Inst 2009;32:1839–45. http://dx.doi.org/10.1016/j.proci.2008.06.052.

[70] Manuputty MY, Lindberg CS, Botero ML, Akroyd J, Kraft M. Detailed characterisation of TiO2 nano-aggregate morphology using TEM image analysis. J Aerosol Sci 2019;133:96–112. http://dx.doi.org/10.1016/j.jaerosci.2019.04.012.

[71] Manuputty MY, Akroyd J, Mosbach S, Kraft M. Modelling TiO2 formation in a stagnation flame using method of moments with interpolative closure. Combust Flame 2017;178:135–47. http://dx.doi.org/10.1016/j.combustflame.2017.01.005.

[72] Dormand J, Prince P. A family of embedded Runge–Kutta formulae. J Comput Appl Math 1980;6:19–26. http://dx.doi.org/10.1016/0771-050X(80)90013-3.

[73] Bieber M, Al-Khatib M, Fröde F, Pitsch H, Reddemann MA, Schmid H-J, et al. Influence of angled dispersion gas on coaxial atomization, spray and flame formation in the context of spray-flame synthesis of nanoparticles. Exp Fluids 2021;62:98. http://dx.doi.org/10.1007/s00348-021-03196-6.

[74] Pitsch H. FlameMaster, a computer code for homogenous combustion and one-dimensional laminar flame calculations: Version 4.2.1. 2022, URL https://www.itv.rwth-aachen.de/downloads/flamemaster/.

[75] Cai L, Pitsch H. Optimized chemical mechanism for combustion of gasoline surrogate fuels. Combust Flame 2015;162:1623–37. http://dx.doi.org/10.1016/j.combustflame.2014.11.018.

[76] Karaminejad S, Dupont SM, Bieber M, Reddemann MA, Kneer R, Dreier T, et al. Characterization of spray parameters and flame stability in two modified nozzle configurations of the SpraySyn burner. Proc Combust Inst 2022. http://dx.doi.org/10.1016/j.proci.2022.07.248.

[77] Schneider F, Suleiman S, Wlokas I, Dreier T, Wiggers H, Schulz C. The SpraySyn standard burner enabling coordinated research on material synthesis in spray flames. In: 29. Deutscher Flammentag. Bochum, Germany; 2019.

[78] Martins FJ, Kirchmann J, Kronenburg A, Beyrau F. Experimental investigation of axisymmetric, turbulent, annular jets discharged through the nozzle of the SPP1980 SpraySyn burner under isothermal and reacting conditions. Exp Therm Fluid Sci 2020;114:110052. http://dx.doi.org/10.1016/j.expthermflusci.2020.110052.

[79] Cifuentes L, Sellmann J, Wlokas I, Kempf A. Direct numerical simulations of nanoparticle formation in premixed and non-premixed flame–vortex interactions. Phys Fluids 2020;32:093605. http://dx.doi.org/10.1063/5.0020979.